DOI: 10.13009/EUCASS2017-269

Icing simulations on engine intake

*Nermin Uğur *, Serkan Özgen *, İlhan Görgülü ** and Volkan Tatar ***

** Middle East Technical University, Dept. Aerospace Eng. Dumlupınar Bul. No:1, 06800, Çankaya, Ankara, Turkey*
*** TUSAŞ Engine Industries Inc. Esentepe Mah. Çevreyolu Bul. No:356, 26003 Tepebaşı, Eskişehir, Turkey*

Abstract

In the present study, the aim is to predict ice accumulation on a 2-D commercial engine intake. The developed tool mainly consists of four modules: modules for the calculation of the flow-field, droplet trajectories and collection efficiencies, thermodynamics and ice accretion. The flow-field solution is done by a panel method modified for the intake geometry and the required engine mass flow rate using a superposition technique. The droplet trajectories are computed using the Lagrangian approach, while the Extended Messinger Model is implemented in the ice accretion module. The results are compared with numerical literature data.

1. Introduction

In-flight ice accumulation on airframes may lead to severe incidents due to degradation in aerodynamic performance and engine power loss. In fact, more than a hundred in-flight incidences have been reported in the last two decades related to icing on aircraft engine components including rollbacks, mechanical failure and flame-outs [10]. Hence, predicting ice accumulation on the airframes is quite crucial in order to detect the regions prone to icing and design de/anti-icing systems for the aircraft as needed. Moreover, simulation of ice accumulation is required for airworthiness certification purposes.

In the present study, a 2-D icing simulation is performed for an engine intake with a computation tool which has been developed for almost ten years and its capabilities have been extended since then. In-flight 2-D icing simulations on airfoil geometries and axisymmetric engine intakes which are performed with this tool are presented in the previous studies of the authors [6], [7], [8].

The experimental and numerical data for ice accumulation on airfoils or wing geometries exist in the literature but such data is rare for geometries like engine nacelles and inlets. In this study, ice shapes calculated on a commercial engine intake have been compared with the numerical data presented by Shen et al. [9]. Although the original coordinates of the intake were not available in the literature, they were obtained by digitizing the 2-D view of the intake available in [9]. Engine nacelles in previous studies of the authors were axisymmetric and the simulations were performed for zero angle of attack cases. The present study aims to explore whether a 2-D approach is adequate when a non-axisymmetric engine intake is considered at a non-zero angle of attack case. The manuscript summarizes the methods used in icing simulations and includes collection efficiency and ice shape results, which are obtained for a non-axisymmetric engine intake for different flight conditions.

2. Methodology

In this section, four modules used in the current approach are explained in detail.

2.1 Flow Field Solution

The intake geometry shown in Figure 1 is studied which is presented in the study of Shen et al. [9] . Due to the lack of coordinates of the commercial intake geometry, they are obtained by digitizing 2-D view given in [9] as in Figure 1. In order to obtain smooth outlines, outer and inner cowls are defined by a super ellipse and ellipse. The intake is non-axisymmetric with an inlet length of 0.824 m and duct height of 1.44 m which are shown in Figure 2.

DOI: 10.13009/EUCASS2017-269

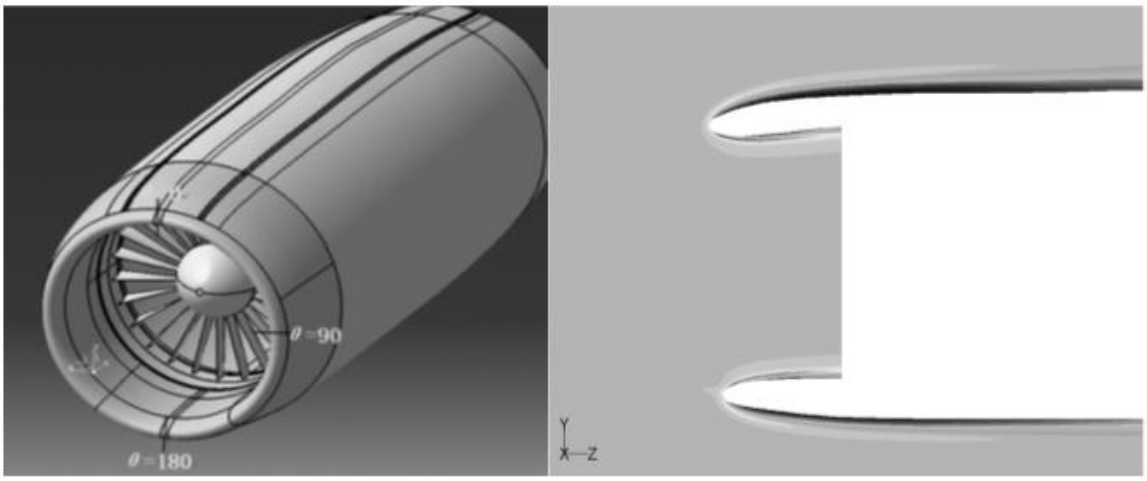

Figure 1: 3-D view (on the left) and 2-D view (on the right) of the commercial engine intake geometry studied [9]

Simulation of the flow through and around the intake using the panel method is complicated because both the required flight conditions and the desired mass flow rate through the intake must be maintained. The desired mass flow rate is achieved at the control plane which is shown in Figure 2. In this study, the desired mass flow rate is calculated in terms of the average control plane velocity in x-direction, denoted by $\overline{U}_{cp}$, the control plane area A_{cp}, and the average local density $\overline{\rho}_{cp}$.

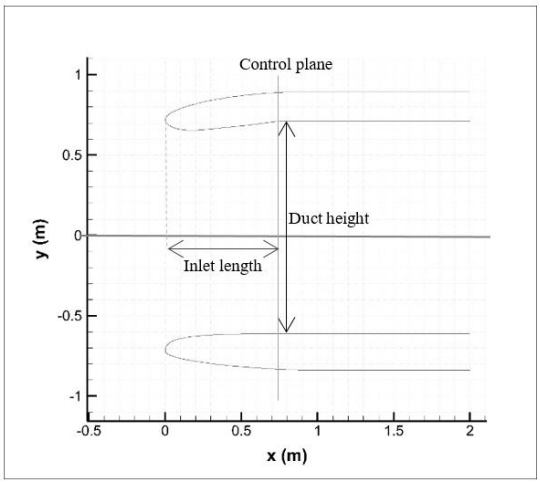

Figure 2 : Modified intake geometry for panel method with constant diameter

The average control plane velocity is calculated by taking the average of the x-component of the velocity vector at 30 evenly distributed points along the control plane. In order to correctly enforce the desired mass flow rate as well as the desired freestream velocity, a superposition procedure described by Waung is used [11]. In this method, the panel geometry is modified as shown in Figure 2 by extending the trailing edge panels in x-direction in order to avoid unrealistic velocity gradients at the trailing edge. With this modified panel geometry, simulating the desired mass flow rate and free stream velocity around the intake is achieved through a combination of two flow situations, illustrated in Figure 3 for a similar geometry to the one studied here.

The first flow situation is the air intake operating at $U_\infty = 1\, m/s$ freestream velocity at α=0^o. The second flow condition is a static flow situation ($U_\infty = 0\, m/s$) where vortex strength along the surface panels are assigned a value of 1, simulating a flow where the freestream velocity is 0, but there is a non-zero mass flow rate at the control plane. The final flow solution is calculated by scaling and combining these two flow situations.

DOI: 10.13009/EUCASS2017-269

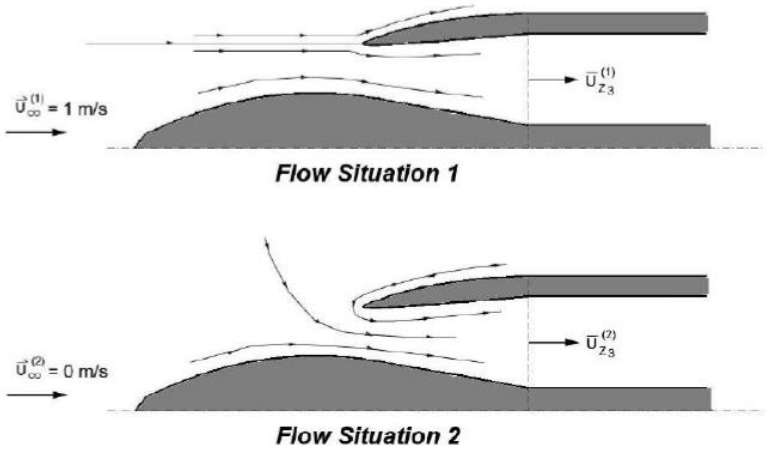

Figure 3 : Visual representation of two flow situations used in the superposition method [11]

2-D Hess-Smith panel method [1] is used to determine flow velocities both on surfaces and in the flow field. The velocity information is required on the surface for boundary-layer calculations in order to obtain heat transfer coefficients and flow field velocities are required for droplet trajectories. In the panel method utilized for the purposes of this study, the geometry is divided into quadrilateral panels each associated with a source singularity element together with a vortex singularity that is constant for all panels. The strengths of the singularities are taken to be constant along each panel and are unknowns of the problem.

The solution procedure for each of the flow situations differ slightly. In order to solve flow situation 1, the developed computer program uses N quadrilateral panels to solve for N+1 singularity strengths using the flow tangency boundary condition at the collocation points of the panels and an additional equation is introduced for the Kutta condition, which is enforced at the leading edge of the intake lip. Flow situation 2 is solved for $U_{\infty} = 0\ m/s$ and Γ = 1. Because the vortex strength is no longer an unknown, the developed computer program uses N quadrilateral panels to solve for N source strengths using the flow tangency boundary condition at the collocation points of the panels without any additional boundary conditions.

The solutions of the two flow situations are scaled using the superposition approach. The combination coefficients are solved using the system of equations below:

$$c_1 U_{\infty 1} + c_2 U_{\infty 2} = U_{\infty} \tag{1}$$

$$c_1 \bar{U}_{cp1} + c_2 \bar{U}_{cp2} = \bar{U}_{cp} \tag{2}$$

Since $U_{\infty 1} = 1\ m/s$ and $U_{\infty 2} = 0$, it follows that $c_1 = U_{\infty}$ and $c_2 = (\bar{U}_{cp} - U_{\infty}\bar{U}_{cp1})/\bar{U}_{cp2}$. Once the singularity strengths are calculated, one can construct a velocity potential and hence calculate the air flow velocity components at any location in the flow field including the boundaries of the geometry. The velocity components at a given point are the x-, y-derivatives of the velocity potential constructed at that point. The results of the panel method also serve the boundary-layer calculations used for the computation of the convective heat transfer coefficients, where the inviscid velocity distribution over the geometry, $U_e(s)$ is required. The velocity components are corrected for compressibility effects using the Prandtl-Glauert compressibility correction:

$$\hat{u} = \bar{u}/\sqrt{1 - M^2}\,, \quad \hat{v} = \bar{v}/\sqrt{1 - M^2}, \tag{3}$$

where $\bar{u}$ and $\bar{v}$ are the perturbation velocity components calculated for incompressible flow and $\hat{u}$ and $\hat{v}$ are the same quantities corrected for compressibility effects.

2.2 Droplet Trajectories and Collection Efficiency Calculations

The following assumptions are used for droplet trajectories:

- Droplets are assumed to be spherical.
- The flow field is not affected by the droplets.

DOI: 10.13009/EUCASS2017-269

- Gravity and aerodynamic drag are the only forces acting on the droplets.
- Heat and mass transfer (evaporation) between the droplet and the surrounding flow are neglected.
- The droplet is assumed to have the same temperature as the flow.
- The local adiabatic recovery temperature at the wall is calculated and imposed as a boundary condition [4].

The droplet trajectories are computed using Lagrangian approach as:

$$m\ddot{x}_p = -D\cos\gamma, \tag{4}$$

$$m\ddot{y}_p = -D\sin\gamma + mg, \tag{5}$$

where

$$\gamma = \tan^{-1}\frac{\dot{y}_p - V_y}{\dot{x}_p - V_x}, \tag{6}$$

$$D = \frac{1}{2}\rho V_{rel}^2 C_D A_p, \tag{7}$$

$$V_{rel} = \sqrt{(\dot{x}_p - V_x)^2 + (\dot{y}_p - V_y)^2} \tag{8}$$

In the above equations, V_x and V_y are the flow velocity components at the droplet location, while $\dot{x}_p$, $\dot{y}_p$, $\ddot{x}_p$ and $\ddot{y}_p$ are the components of the droplet velocity and acceleration. The symbols ρ and A_p denote the atmospheric density and cross-sectional area of the droplet. C_D denotes the particle drag coefficient. In the present study, the following formulation is employed for drag coefficients [2]:

$$C_D = \frac{24}{Re}(1 + 0.197Re^{0.63} + 2.6 * 10^{-4}Re^{1.38}), \quad Re \leq 3500, \tag{9}$$

$$C_D = \frac{24}{Re}(1.699 * 10^{-5})Re^{1.92}, \quad Re > 3500. \tag{10}$$

In the above formulation, $Re = \rho V_{rel} d_p/\mu$ is the Reynolds number based on droplet diameter d_p and relative velocity V_{rel}. The viscosity μ is calculated using Sutherland's law as a function of temperature.

Trajectory calculations start from an upstream location far away from the leading edge so that air flow velocity components are sufficiently close to their freestream values. The initial droplet velocity is taken to be the terminal velocity:

$$V_{term}^2 = \frac{4}{3}\frac{(\rho_w - \rho)}{\rho}\frac{g d_p}{C_D}. \tag{11}$$

The droplet trajectories are obtained by integrating equations (4) and (5) over time until the droplet impacts the geometry or misses it. The droplet impact pattern on the section determines the amount of water that impinges on the surface and the region subject to icing. The local collection efficiency is defined as the ratio of the area of impingement to the area through which water passes at some distance upstream of the section, $\beta = A_o/A$.

2.3 Thermodynamic Analysis

When the collection efficiency distribution around the geometry is determined, the convective heat transfer coefficients need to be calculated for the thermodynamic analysis. The boundary-layer calculations are done by solving the two-dimensional Integral Boundary Layer equation. The boundary-layer calculations start at the stagnation point at the leading edge and proceed downstream using the marching technique for the outer and inner surfaces of the inlet. This method enables calculation of the details of the laminar and turbulent boundary layers fairly accurately. The same method used by Özgen and Canıbek [5] can be used. According to this method, the convective heat transfer coefficients in the laminar flow region are calculated employing the method of Smith and Spaulding [2]:

$$h_c = \frac{0.296kU_e^{1.435}}{\sqrt{\nu\int_0^s U_e^{1.87}ds}}, \tag{12}$$

where k is the thermal conductivity of air. The convective heat transfer coefficient in the turbulent region is computed using the method of Kays and Crawford [2]:

$$h_c = St\rho U_e C_p, \tag{13}$$

where C_p is the specific heat of air and St is the Stanton number.

DOI: 10.13009/EUCASS2017-269

Transition from laminar to turbulent flow occurs when the Reynolds number based on roughness height exceeds $Re_k = 600$, where $Re_k = \rho U_k k_s/\mu$, with k_s being the roughness height and U_k being the local flow velocity at the roughness height, for details see [5].

2.4 Extended Messinger Model

Ice accretion on the geometry is obtained with the Extended Messinger Method. The ice shape prediction is based on phase change or the Stefan problem. The governing equations for the phase change problem are mainly: energy equations in the ice and water layers, mass conservation equation and a phase change condition at the ice/water interface [3].

$$\frac{\partial T}{\partial t} = \frac{k_i}{\rho_i C_{pi}} \frac{\partial^2 T}{\partial y^2} \tag{14}$$

$$\frac{\partial \theta}{\partial t} = \frac{k_w}{\rho_w C_{pw}} \frac{\partial^2 \theta}{\partial y^2} \tag{15}$$

$$\rho_i \frac{\partial B}{\partial t} + \rho_w \frac{\partial h}{\partial t} = \rho_a \beta V_\infty + \dot{m}_{in} - \dot{m}_{e,s} \tag{16}$$

$$\rho_i L_F \frac{\partial B}{\partial t} = k_i \frac{\partial T}{\partial y} - k_w \frac{\partial \theta}{\partial y} \tag{17}$$

In equations 14-17, θ and T are the temperatures, k_w and k_i are the thermal conductivities, C_{pw} and C_{pi} are the specific heats and h and B are the thicknesses of water and ice layers, respectively. On the other hand, ρ_i and L_F denote the density of ice and the latent heat of solidification of water, respectively. Ice density is assumed to have different values for rime ice, ρ_r and glaze ice, ρ_g. The coordinate y is normal to the surface and ρ_a is the liquid water content.

In equation (16), $\rho_a \beta V_\infty$, $\dot{m}_{in}$ and $\dot{m}_{e,s}$ are impinging, runback and evaporating (or sublimating) water mass flow rates for a control volume, respectively. The boundary and initial conditions accompanying equations (14-17) are:

- Ice is in perfect contact with the wing surface:

$$T(0,t) = T_s \tag{18}$$

The surface temperature is taken to be the recovery temperature [2]:

$$T_s = T_a + \frac{V_\infty^2 - U_e^2}{2C_p} \frac{1+0.2rM^2}{1+0.2M^2} \tag{19}$$

In the above expression, $M = V_\infty/a_\infty$, while the speed of sound is given by $a_\infty = \sqrt{\gamma R T_a}$. Additionally, r is the adiabatic recovery factor.

- The temperature is continuous at the ice/water boundary and is equal to the freezing temperature, T_f :

$$T(B,t) = \theta(B,t) = T_f \tag{20}$$

- At the air/water (glaze ice) or air/ice (rime ice) interface, heat flux is determined by convection, radiation, latent heat release, cooling by incoming droplets, heat brought in by runback water, evaporation or sublimation, aerodynamic heating and kinetic energy of incoming droplets.

- Surface is initially clean:

$$B = h = 0, \quad t = 0 \tag{21}$$

In the current approach, each panel constituting the geometry is also a control volume. The above equations are written for each panel and ice is assumed to grow perpendicularly to a panel.

Rime ice growth is expressed with an algebraic equation from the mass balance in equation (16), since water droplets freeze entirely on impact:

$$B(t) = \frac{\rho_a \beta V_\infty}{\rho_r} t \tag{22}$$

DOI: 10.13009/EUCASS2017-269

On the other hand, glaze ice thickness is obtained by integrating the ordinary differential equation obtained by combining mass and energy equations over time. The differential equation is:

$$\rho_g L_f \frac{\partial B}{\partial t} = \frac{k_i(T_f - T_s)}{B} + k_w \frac{(Q_c+Q_e+Q_d+Q_r)-(Q_a+Q_k)}{k_w + h\frac{Q_c+Q_e+Q_d+Q_r}{T_s-T_a}} - Q_{ent} \tag{23}$$

In this expression, Q_c is heat flux by convection, Q_e is evaporation, Q_d is heat from incoming droplets, Q_r is radiation, Q_a is aerodynamic heating, Q_k is kinetic energy of incoming droplets and Q_{ent} is the energy entering the control volume due to runback water. It is assumed that, all of the unfrozen water passes to the neighboring downstream cell for the upper surface, while all water sheds for the lower surface[8]. To calculate the glaze ice thickness, equation (23) is integrated numerically, using a Runge-Kutta-Fehlberg method.

3. Results and Discussion

In this section, predicted ice shape results are presented for the commercial aircraft intake geometry. The results are compared with the numerical data presented by Shen et al. [9] which are obtained with FENSAP-ICE commercial tool and developed code by the authors. The analyses are performed at a Mach number of 0.4, ambient pressure of 101325 Pa, angle of attack of 3°, median volumetric diameter of 20 μm, liquid water content of 1 g/m^3 and mass flow rate of 200 kg/s. Two different cases with temperature (T) of 253°K and 263°K are analyzed. The exposure time for both cases is 420 s.

Ice shape results for T=253°K are given in Figure 4 and Figure 5 for upper and lower lips of the intake, which are stated as θ=0° and θ=180° respectively in Figure 1. Temperature of 253°K corresponds to rime ice condition which is formed in a way that follows the geometry contours. Therefore, rime ice can be said to be less hazardous than glaze ice in terms of aerodynamic performance loss since the profile is changed less with ice formation.

For the upper surface, accumulated ice is predicted smaller when compared to reference numerical data. Impingement limits differ for current study and reference data. Current study result shows a smaller region occupied by the accumulated ice. However, ice shape can be said to be similar to the one obtained by Shen et al. although the limits are underestimated.

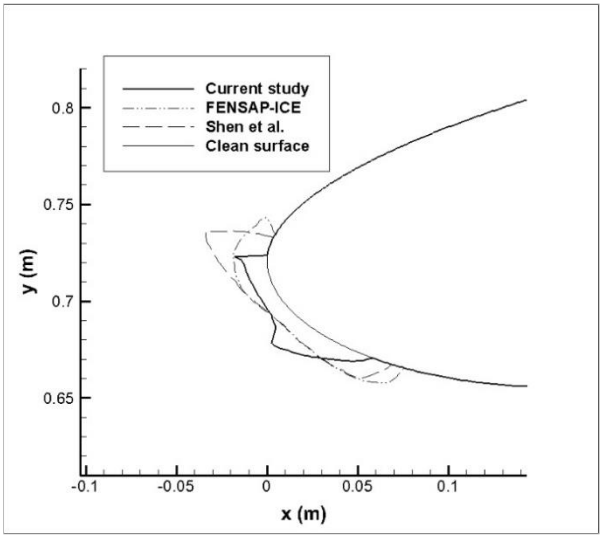

Figure 4: Ice shape prediction on the upper lip at T=253°K

In Figure 5, ice shape is given for the lower lip of the intake. It is observed that impingement limit in the lower part of the lip is predicted the same with the reference numerical data although the upper impingement limit is estimated different which leads to the prediction of the iced region to be smaller for the current study. Ice thickness is predicted very similar when compared to reference numerical data except for the sharp section in the upper region of the leading edge. It is clear that flow field is affected by the ice accumulated on the lower surface since the angle of attack is 3°.

DOI: 10.13009/EUCASS2017-269

Therefore, ice shape predicted on the lower surface will have an effect on ice shape on the upper surface as well. It can be deduced that the sharp ice section accumulated on the lower surface may lead the ice mass on the upper surface to be underestimated.

The second flight condition at which the icing analysis are performed is at T=263ºK. This temperature corresponds to glaze ice condition. Glaze ice is typically in irregular shape which leads to significant aerodynamic performance degradation since the profile is changed. Since the ambient temperature is high, unfrozen liquid acts like runback water and freezes downstream of the surface. Therefore, glaze ice thickness is smaller than rime ice although the region occupied by the ice is larger.

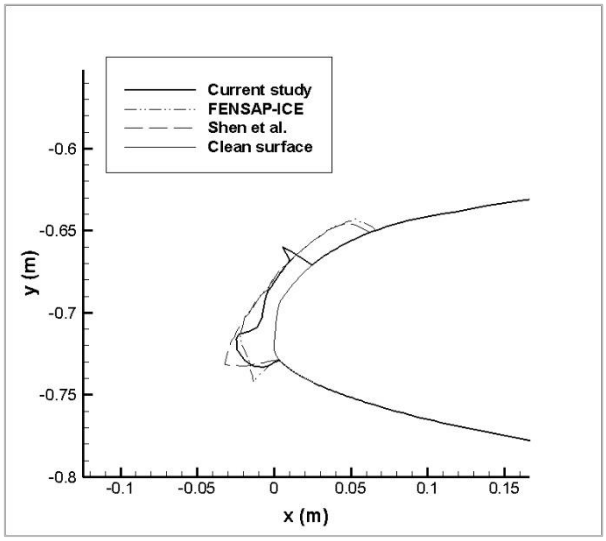

Figure 5: Ice shape prediction on the lower lip at T=253ºK

Figure 6 depicts ice shape predictions on the upper surface for T=263ºK. Ice shape can be said to be similar considering the sharp edge on the top and the ice thickness for the current study result and reference numerical data. However, it is observed that impingement limits especially in lower part are estimated poorly in the present study.

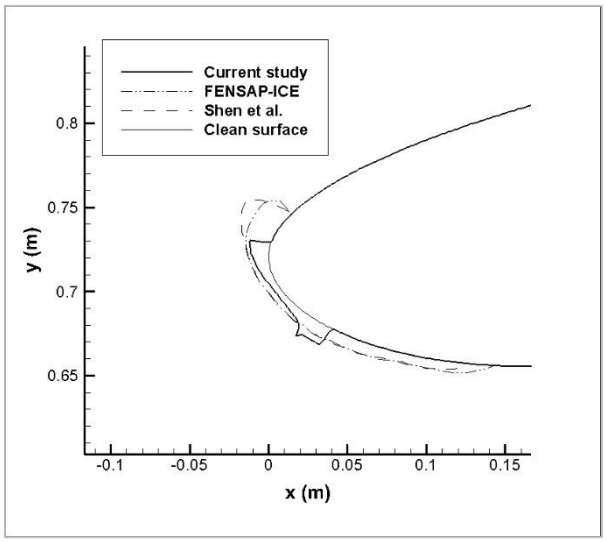

Figure 6: Ice shape prediction on the upper lip at T=263ºK

DOI: 10.13009/EUCASS2017-269

In Figure 7, ice shape results on the lower surface are presented. Similar to upper surface, impingement limits are not predicted well compared to reference results. Ice thickness is estimated thicker in the current study. The ice shape is in horn-like shape which is a glaze ice characteristic; however, it is quite different than reference numerical data.

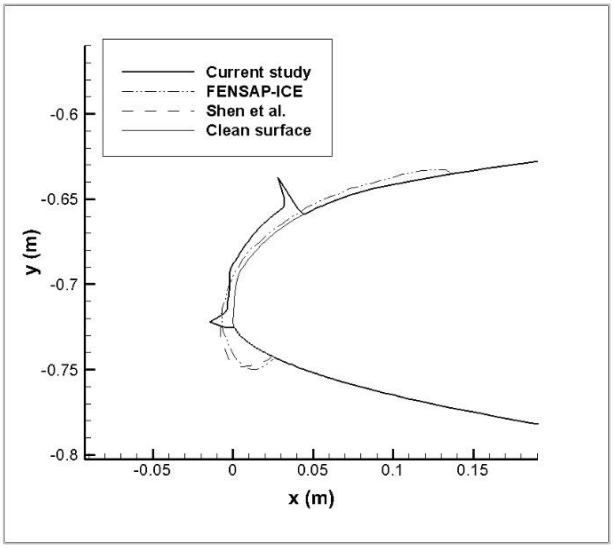

Figure 7: Ice shape prediction on the lower lip at T=263ºK

Multi-step calculation approach is used in the icing analyses. In this approach, the exposure time is divided into shorter intervals and the computational procedure is repeated for each interval. At the beginning of each interval, iced surface is considered as the new geometry. In previous studies of the authors [7], [8], it is observed that multi-step calculation approach improves ice shape predictions as exposure time increases and for especially glaze ice conditions. On the other hand, after trying different numbers of calculation steps for the engine intake icing analyses, it is noticed that single-step calculation gives the best ice shape result. The reason behind this can be explained by the fact that the method applied in the current study is not applicable for icing calculations on non-axisymmetric intake at non-zero angle of attack. Dividing exposure time into intervals causes to diverge from the correct ice shape on engine intake rather than enhancing as in axisymmetric intake case at zero angle of attack.

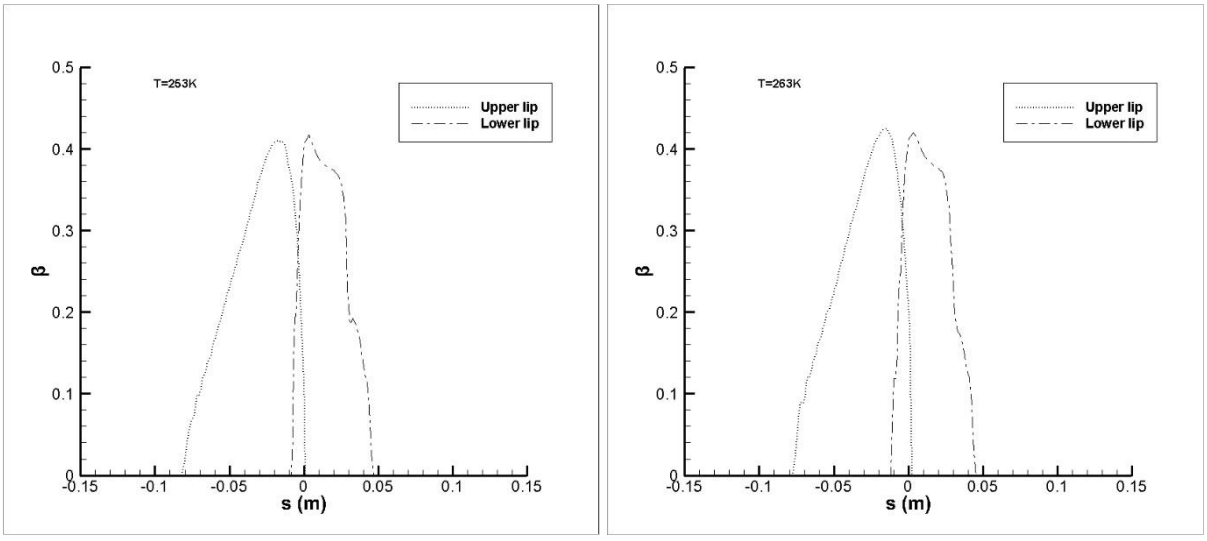

Figure 8: Collection efficiency (β) on upper and lower lips at T=253ºK (on the left) and T=263ºK (on the right)

As mentioned in Methodology section, Lagrangian approach is utilized for droplet trajectory calculations. Collection efficiency distribution on upper and lower lips are presented in

DOI: 10.13009/EUCASS2017-269

Figure 8 at at T=253ºK and T=263ºK. Negative s values represents lower part of the lip whereas positive s values represents upper part of the lip. Collection efficiencies for two cases are very similar. Maximum collection efficiency, β, is calculated as around 0.42 which is observed at the stagnation point of the intake lip for both cases. In the reference paper by Shen et al. [9], maximum collection efficiency is said to be found as 0.42 with Eulerian approach without indicating the flight condition. Despite different trajectory methods, maximum collection efficiency values are found the same. Lack of collection efficiency distribution in the reference data prevents further comparisons to be done.

4. Conclusion

2-D icing simulations on a non-axisymmetric intake geometry are performed for two different test cases. In the current study, the approach which has been validated for axisymmetric intake geometries at zero angle of attack cases in previous studies is investigated for its applicability to non-axisymmetric geometries at non-zero angle of attack. Ice shape prediction and collection efficiency results are presented which are compared with reference numerical data. The results show that ice shape for rime ice condition is predicted better when compared to glaze ice condition. Ice mass accumulated on the surfaces is estimated less than the one predicted in the reference study. Ice shape which is formed on the lower surface can be said to be more consistent with numerical data than upper surface. Impingement limit predictions are poor in the current study which estimate narrower regions occupied by the ice on the surfaces. It is remarked that reference data are obtained with three-dimensional approach and current two-dimensional approach seems inadequate although it is faster. In the light of these results, it is deduced that present approach used in the icing calculations is not sufficient to predict ice shape formed on non-axisymmetric intakes at non-zero angle of attack cases. In order to obtain more accurate ice shapes formed on non-axisymmetric engine intakes, three-dimensional approach is suggested despite higher CPU time.

References

[1] Cebeci, T., 1999. An Engineering Approach to the Calculation of Aerodynamic Flows, Springer-Verlag,

[2] Gent, R.W., Dart, N.P. and Cansdale, J.T., 2000. *Aircraft Icing, Phil. Trans. R. Soc. Lond. A*, Vol. 358, p: 2873-2911

[3] Myers, T.G., 2001. Extension to the Messinger Model for aircraft icing, *AIAA J.*, Vol. 39, pp. 211-218

[4] Özgen, S., Tarhan, E., Canıbek, M., 2011. Parallel Computing Applied to Three-Dimensional Droplet Trajectory Simulation in Lagrangian Approach, In: SAE International Conference on Aircraft and Engine Icing and Ground Deicing, Chicago

[5] Özgen, S. and Canıbek, M., 2012. In-Flight Ice Formation Simulation on Finite Wings and Nacelles, *Aeronautical J.*, Vol. 116(1177), p: 337-362

[6] Özgen, S., Uğur, N., Görgülü, İ. and Tatar, V., 2015. Ice Accretion Simulations on Airfoils, In: 6th European Conference for Aeronautics and Space Sciences (EUCASS), Cracow

[7] Özgen, S., Uğur, N., Görgülü, İ. and Tatar, V., 2015. Ice Accretion Prediction on an Engine Inlet, In: Ankara International Aerospace Conference (AIAC), Ankara

[8] Özgen, S., Uğur, N., Görgülü, İ. and Tatar, V, 2015. Ice Accretion Prediction on Engine Nacelles in Liquid Phase Clouds, In: SAE International Conference on Icing of Aircraft Engines and Structures, Prague

[9] Shen, X., Lin, G., Yu J., Bu X., and Du C., 2013. Three-Dimensional Numerical Simulation of Ice Accretion at the Engine Inlet, *Journal of Aircraft*, Vol. 50, No. 2

[10] Villedieu, P., Trontin, P., and Chauvin, R.,2014. Glaciated and Mixed Phase Ice Accretion Modeling Using ONERA 2D Icing Suite, In: 6th AIAA Atmospheric and Space Environments Conference, Atlanta, AIAA 2014-2199

[11] Waung, T.S., 2010. An Ejector Inlet Design Method for a Novel Rocket-Based Combined-Cycle Rocket Nozzle. M.Sc. Thesis. Ottawa-Carlton Institute for Mechanical and Aerospace Engineering